OPTICS

Nonlinear up-conversion of a polarization Möbius strip with half-integer optical angular momentum

Martin Luttmann[1]*, Mekha Vimal[1], Matthieu Guer[1,2], Jean-François Hergott[1], Antonio Z. Khoury[3], Carlos Hernández-García[2], Emilio Pisanty[4], Thierry Ruchon[1]*

Symmetries and conservation laws of energy, linear momentum, and angular momentum play a central role in nonlinear optics. Recently, paraxial light fields with nontrivial topology have been attracting a keen interest. Despite not being eigenstates of the orbital and spin angular momenta (OAM and SAM), they are eigenstates of the generalized angular momentum (GAM) operator—a mixture of the OAM and SAM operators with fractional eigenvalues. By driving high harmonic generation with a polarization Möbius strip carrying a half-integer GAM charge and implementing angular momentum characterization methods in the extreme ultraviolet range, we demonstrate the linear scaling of the GAM with the harmonic order, each harmonic carrying a precise half-integer GAM charge. Our work shows that beyond SAM and OAM, the GAM is, in some situations, an appropriate quantum number. It paves the way for finer manipulations and applications of light beams containing fractional-order polarization singularities.

INTRODUCTION

Beyond bosons and fermions, which respectively carry integer and half-integer values of spin angular momentum (SAM), quantum particles whose motion is confined in two dimensions can exhibit intriguing angular momentum quantizations. For instance, charge carriers obey "anyonic" (i.e., neither bosonic nor fermionic) statistics in the fractional quantum Hall effect (*1*). Similarly, as one particular direction is determined by their propagation axis, paraxial light beams do not show any full three-dimensional (3D) rotational symmetry. Ballantine *et al.* (*2*) recently demonstrated that, although photons are classified as bosons, light beams that are superposition states of different orbital angular momentum (OAM) and SAM can be described in terms of an angular momentum operator with noninteger eigenvalues. For instance, light fields that are invariant under a rotation of the spatial dependence by an angle ϕ, followed by a rotation of the polarization vector by a fraction $\gamma\phi$ of that angle—a transformation called coordinated rotation (*3*)—are eigenvectors of the generalized angular momentum (GAM): $J_{z,\gamma} = L_z + \gamma S_z$, with $J_{z,\gamma}$, L_z, and S_z the projections of the GAM, OAM, and SAM operators along the propagation axis z. Depending on the value of γ, $J_{z,\gamma}$ has integer or half-integer eigenvalues, the latter yielding a fermionic-like spectrum. Coordinated rotation invariant monochromatic light fields are topologically equivalent to twisted ribbons if γ is an integer or Möbius strips (*4*–*6*) if it has a half-integer value. In the more general situation of polychromatic fields, the eigenvalues of $J_{z,\gamma}$ can be arbitrary rational numbers. In this case, the topology of the corresponding light beam and of the symmetry group is that of a torus knot (*3*) so that the GAM can be identified as a torus knot angular momentum. The GAM formalism provides a relevant alternative to the usual descriptions relying on "fractional OAM" states (*7*, *8*).

The conservative nature of the GAM, which remains experimentally unexplored, is expected to find a rich scenario in nonlinear optics (*8*, *9*). While several earlier works have tackled OAM and SAM conservation separately, very few have investigated experimentally the case where the fundamental field is a superposition of both forms of angular momentum. An exception is the recent report of the up-conversion of vector-vortex beams (*10*) associated to the integer-valued total angular momentum $L_z + S_z$ and interpreted in terms of the Pancharatnam charge. However, the complete characterization of the angular momentum content of light beams up-converted from a half-integer GAM eigenstate raises specific experimental difficulties, which thus far prevented their investigation.

In this article, we demonstrate the linear scaling of a half-integer GAM charge with the harmonic order in a nonlinear optical process. This investigation must use an isotropic and homogeneous nonlinear medium because both SAM and OAM have to be conserved separately. Common nonlinear crystals are generally birefringent and do not have the required rotational invariance, yielding transfers of angular momentum between light and matter or optical spin-orbit coupling (*11*, *12*). Alternatively, simultaneous OAM and SAM conservation is precisely achievable in high-order harmonic generation (HHG), a highly nonperturbative nonlinear optical process occurring in gases (*13*–*20*). Here, we report on HHG driven by a planar polarization Möbius strip with GAM charge $j_\gamma^{IR} = 1/2$, which is formed by superimposing two infrared (IR) driving beams carrying different OAM and SAM. A major challenge faced in this program is the characterization of the OAM carried by the extreme ultraviolet (XUV) harmonics. The techniques commonly used in the visible domain based on interference or mode conversion with tilted lenses are difficult or impossible to implement here because of the absence of transmissive optics at XUV wavelengths. We instead propose two methods. The first is based on spatial interference between two harmonic vortices and allows retrieval of their relative phase variation. The second uses transverse mode conversion by a spherical mirror (*21*–*23*), which had not been achieved in the XUV domain so far. Both techniques

[1]Université Paris-Saclay, CEA, CNRS, LIDYL, Gif-sur-Yvette 91191, France. [2]Grupo de Investigación en Aplicaciones del Láser y Fotónica, Departamento de Física Aplicada, University of Salamanca, Salamanca E-37008, Spain. [3]Instituto de Física, Universidade Federal Fluminense, Niterói, RJ 24210-346, Brazil. [4]Department of Physics, King's College London, Strand Campus, London WC2R 2LS, UK.
*Corresponding author. Email: martin.luttmann@cea.fr (M.L.); thierry.ruchon@cea.fr (T.R.)

might be promising in future experiments involving XUV beams with angular momentum.

RESULTS

GAM formalism

We begin by defining the operator $J_{z,\gamma} = L_z + \gamma S_z$ in such a way that nonseparable superpositions of SAM and OAM modes can be treated as eigenstates (*2*). We consider nonseparable states, or spin-orbit states (*24*), of the form

$$|\psi_{SO}\rangle = \frac{|\ell_1\rangle|\sigma = 1\rangle \pm |\ell_2\rangle|\sigma = -1\rangle}{\sqrt{2}} \quad (1)$$

where $\ell_{1,2}$ and σ denote the eigenvalues of the OAM and SAM operators, respectively. We note that $|\psi_{SO}\rangle$ is an eigenstate of the total angular momentum $J_z = L_z + S_z$ only in the specific case where $\ell_2 - \ell_1 = \pm 2$. Radially and azimutally polarized beams fall into this category (*10*). Instead, applying the more general $J_{z,\gamma}$ operator, we obtain

$$J_{z,\gamma}|\psi_{SO}\rangle = \frac{(\ell_1 + \gamma)|\ell_1\rangle|\sigma = 1\rangle \pm (\ell_2 - \gamma)|\ell_2\rangle|\sigma = -1\rangle}{\sqrt{2}} \quad (2)$$

$|\psi_{SO}\rangle$ is an eigenstate of $J_{z,\gamma}$ provided that $\ell_1 + \gamma = \ell_2 - \gamma$. Thus, any nonseparable state of the type of Eq. 1 is an eigenstate of $J_{z,\gamma}$ with

$$\gamma = \frac{\ell_2 - \ell_1}{2} \quad (3)$$

and the corresponding eigenvalue is $j_\gamma = \frac{\ell_1 + \ell_2}{2}$. Depending on the value of γ, $J_{z,\gamma}$ thus has integer or half-integer eigenvalues, the latter case corresponding to the Möbius strip topology.

Theoretical model of HHG with a polarization Möbius strip

Here, we use a high-intensity IR polarization Möbius strip field to drive HHG in a jet of argon gas. This field is obtained by overlapping, temporally and spatially, the pulses from two 800-nm wavelength laser beams (referred to as beams 1 and 2) carrying the OAM charges $\ell_1 = 0$ and $\ell_2 = 1$ and the opposite SAM (i.e., they have orthogonal circular polarization) $\sigma_1 = +1$ and $\sigma_2 = -1$ (*6*). According to Eq. 3, the associated coordination factor is thus $\gamma = \frac{1}{2}$, and both driving beams carry the same half-integer GAM charge: $j_\gamma^{IR} = \ell_1 + \gamma\sigma_1 = \ell_2 + \gamma\sigma_2 = \frac{1}{2}$. Thus, the total IR field is a GAM eigenstate despite the fact that it is not an eigenstate of the SAM and OAM operators. Figure 1A shows the IR polarization state in the transverse plane when the two driving beams are collinear. On the optical axis, the polarization is purely circular, forming a "C point" (*25*, *26*). Around the C point, the field is elliptically polarized, and the orientation of the ellipse varies by π when travelling along a loop about the optical axis (Fig. 1A). The winding number associated to the C point is thus equal to 1/2 (*5*). To visualize the Möbius strip topology of the field, the polarization ellipses computed along the gray dashed circle in Fig. 1A are stacked, resulting in a twisted strip traced by the major axis of the ellipses, the two ends of which corresponds to the azimuth 0 and 2π. Connecting them, we obtain a Möbius strip whose single edge is traced by the tips of the ellipses (Fig. 1B). Note that because we are dealing with paraxial light beams, this Möbius strip only exists in a synthetic space rather than in real space. The interaction of this IR field with the atomic gas results in the emission of high-order odd harmonics. Because the efficiency of the process decreases exponentially with the ellipticity of the driving field (*27*), XUV emission mostly occurs along the circle where beams 1 and 2 have equal intensity, i.e., where the IR polarization is linear (Fig. 1A and fig. SB).

We model HHG using the so-called thin-slab model (Materials and Methods). The results are displayed in Fig. 1C. Each harmonic is itself a polarization Möbius strip (top), i.e., is a superposition of OAM and SAM states. This can be understood within a parametric picture of HHG. To emit the qth harmonic, with q odd, p photons can be taken from beam 1 and $q - p$ photons from beam 2. OAM conservation (*16*–*19*, *28*, *29*) implies that the resulting emission channel (q, p) carries the OAM $\ell^{(q,p)} = p\ell_1 + (q - p)\ell_2 = q - p$. SAM conservation forbids all photonic channels yielding an XUV photon with spin $\sigma^{(q,p)} \neq \pm 1$ (*30*, *31*). Thus, each harmonics is expected to be a superposition of two emission channels, which we refer to with "+" and "−" subscripts, carrying the SAM $\sigma_\pm^{(q)} = \pm 1$ and the OAM $\ell_\pm^{(q)} = (q \mp 1)/2$ (*8*). Such a photon picture also predicts that the GAM charge of harmonic q should be $j_\gamma^{(q)} = \ell_+^{(q)} + \gamma\sigma_+^{(q)} = \ell_-^{(q)} + \gamma\sigma_-^{(q)} = q/2$. In the time domain, the GAM conservation corresponds to invariance under a dynamical symmetry consisting of a coordinated rotation and a time delay (*32*). Inspecting the complex XUV field E, this linear increase of the GAM with the harmonic order appears when we plot the so-called rectifying phase, defined as $\Phi = \frac{1}{2}\arg(E \cdot E)$ (*33*). It shows $2 \times j_\gamma^{(q)}$ phase jumps of π (Fig. 1C, bottom).

Experimental results

To experimentally verify these predictions, one has to access the SAM and OAM content of the high harmonics. The spatially resolved measurement of the polarization and OAM state of those composite beams would be extremely challenging because of the cumbersome operation of phase retarders (*30*, *34*, *35*) and Hartman sensors (*19*, *36*) in the XUV. Here, we instead lift the degeneracy of the two $\sigma^{(q)} = \pm 1$ emission channels by introducing a small angle θ (50 mrad) between the two driving IR beams. This way, the two channels are separated angularly, as shown in Fig. 1F, as a consequence of the conservation of the photon linear momentum (*37*, *38*). Because of the noncollinear crossing of the drivers, the IR polarization Möbius strip now exhibits several right- and left-handed twists (Fig. 1, D and E, and movie S1). Still, the net number of twists remains one, i.e., one can untwist the Möbius strip of Fig. 1E to obtain that of Fig. 1B, as a consequence of the topological protection of the winding number (*5*).

In the first step of the experiment, we set the polarization of the two superimposed IR beams to linear vertical while keeping their OAM equal to $\ell_1 = 0$ and $\ell_2 = 1$. In this configuration, the emission of all HHG photon channels (q, p) is allowed. This process corresponds to HHG driven by a fork-shaped intensity and phase grating, making it possible to draw an analogy with holography (*18*). The measured XUV spectrum is shown in Fig. 2A. The noncollinear angle θ was adjusted so that, for harmonic 11, the bottom part of the beamlet (q, p) spatially overlaps with the top part of the one after, $(q, p + 1)$. In the overlapping region, the spatial phases of the two neighboring vortices vary in opposite directions, and an interference pattern can be observed (Fig. 2B). As we consider higher values of p, the OAM gets higher; thus, the spatial period of the interference pattern gets smaller. Comparing with simulation results

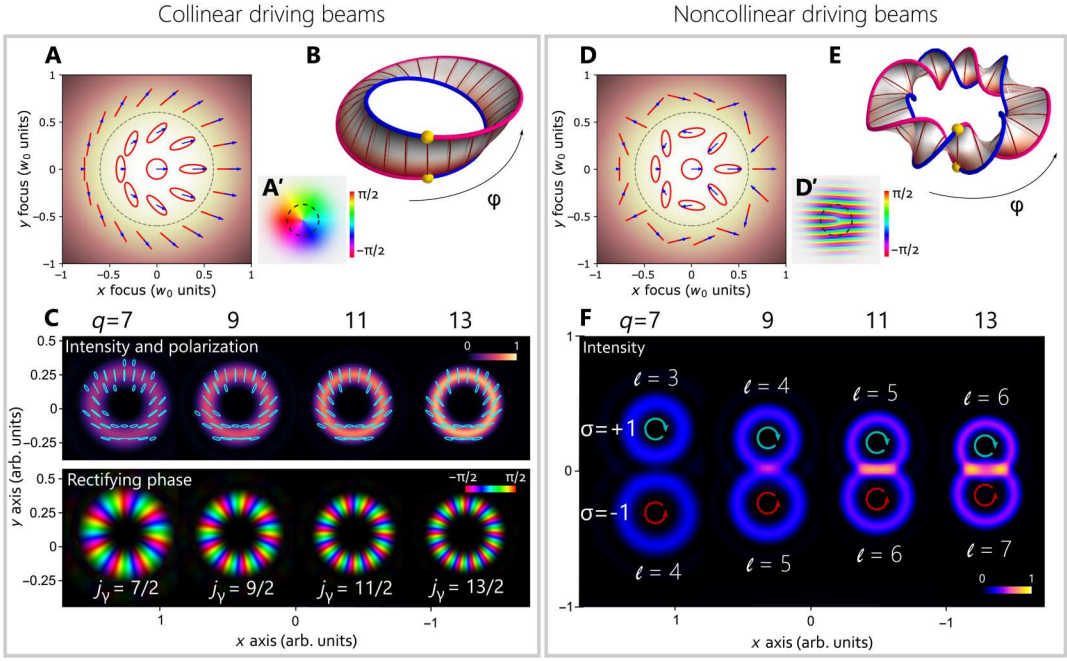

Fig. 1. Möbius strip topology of the driving IR field and corresponding simulated XUV spectra. Left: Collinear driving beams. Right: Noncollinear driving beams (relative angle θ = 50 mrad). (**A** and **D**) Polarization state of the total IR driving field (red curves) and electric field at time $t = 0$ (blue arrows) for three different raddi. The background color map displays the field intensity. (A′ and D′) Orientation angle of the IR polarization ellipse. (**B** and **E**) Möbius strip constructed by stacking the IR polarization ellipses along the dashed circle in (A) and (D) and connecting those corresponding to $\phi = 0$ and $\phi = 2\pi$. The blue and pink lines trace the path of the tip of the ellipse over a 2π range of the azimuthal angle ϕ. The yellow spheres indicate the connecting points of these two curves. (**C**) Simulated far field harmonics. The top shows the intensity and polarization state (cyan ellipses). The bottom displays the rectifying phase, defined as $\arg(E \cdot E)/2$, where E is the complex Fourier amplitude of the harmonic. The GAM charge $j_\gamma = \ell + \gamma\sigma = \ell + \frac{1}{2}\sigma$ corresponds to the number of azimuthal π phase jumps divided by 2. (**F**) Simulated far field XUV intensity. The blue (respectively red) arrows represent $\sigma = +1$ (respectively $\sigma = -1$) SAM states.

(Fig. 2, C and D), the periodicity of the interference fringes provides a measurement of the absolute value of the algebraic sum of the two OAM charges (see the "Rescaling of the far field image" and "Interference of two linearly polarized XUV vortices" sections in Supplementary Text). The result is compatible with the predicted law $\ell^{(q,p)} = q - p$. Note that the interference pattern is also clearly visible for harmonics 9 and 13 (see the "Line outs of the vortex interference for harmonics 9 and 13" section in Supplementary Text). Incidentally, this experiment allows us to observe the interference between two distinct photonic channels of a given harmonic. In particular, it could provide a way to retrieve their relative phase, which, to the best of our knowledge, was not achieved thus far. This unique capability is provided by the azimuthal phase variation and the high divergence of OAM beams.

We then set the polarization of the driving beams to counter-rotating circular and generate high harmonics with the resulting polarization Möbius strip. We obtain the harmonic spectrum shown in Fig. 3A. As expected, all beamlets are completely extinguished, except for the two located about the bisector of the drivers, for all harmonic orders. Comparing with Fig. 2A, we also observe complete suppression of the interference fringes in the overlapping region of the vortices. These two facts indicate that the remaining beamlets have opposite ±1 SAM, inherited from the driving IR beams, and that the interference pattern now takes the form of a complex rotating polarization direction in the region where they overlap. As a downside, it is now impossible to quantify the OAM content with the previous method. Instead, we take advantage of controllable astigmatism of the refocusing optics. By increasing the incidence angle of the XUV light on a spherical mirror (Materials and Methods) from normal up to 15°, we obtain a partial Laguerre-Gaussian (LG)–to–Hermite-Gaussian (HG) mode converter (see the "Partial LG to HG mode conversion" and "Mode conversion with linearly polarized harmonics" sections in Supplementary Text) (*21*–*23*). Counting the number of intensity minima on the diagonal of each harmonic vortex (Fig. 3, B and D) (*39*), we find that the beamlets $[q, (q \pm 1)/2]$ carry the OAM $(q \mp 1)/2$, in agreement with the OAM value measured with linear polarization and the prediction of the photon counting method. With the values of both the OAM and SAM of the high-harmonic vortices in hand, we can now compute their GAM charge. According to the experimental and theoretical results, the channels of harmonic order q carry the OAM $\ell_\pm^{(q)} = (q \mp 1)/2$ and the SAM $\sigma_\pm^{(q)} = \pm 1$. Thus, despite having different OAM charges and helicities, they both carry the same GAM charge

$$j_\gamma^{(q)} = \ell_\pm^{(q)} + \gamma\sigma_\pm^{(q)} = \frac{q}{2} \tag{4}$$

The GAM charge is therefore a property of harmonic q, which does not depend on the number of photons absorbed from each driving IR beam. It is equal to q times that of the fundamental beams

$$j_\gamma^{(q)} = q \times j_\gamma^{\mathrm{IR}} \tag{5}$$

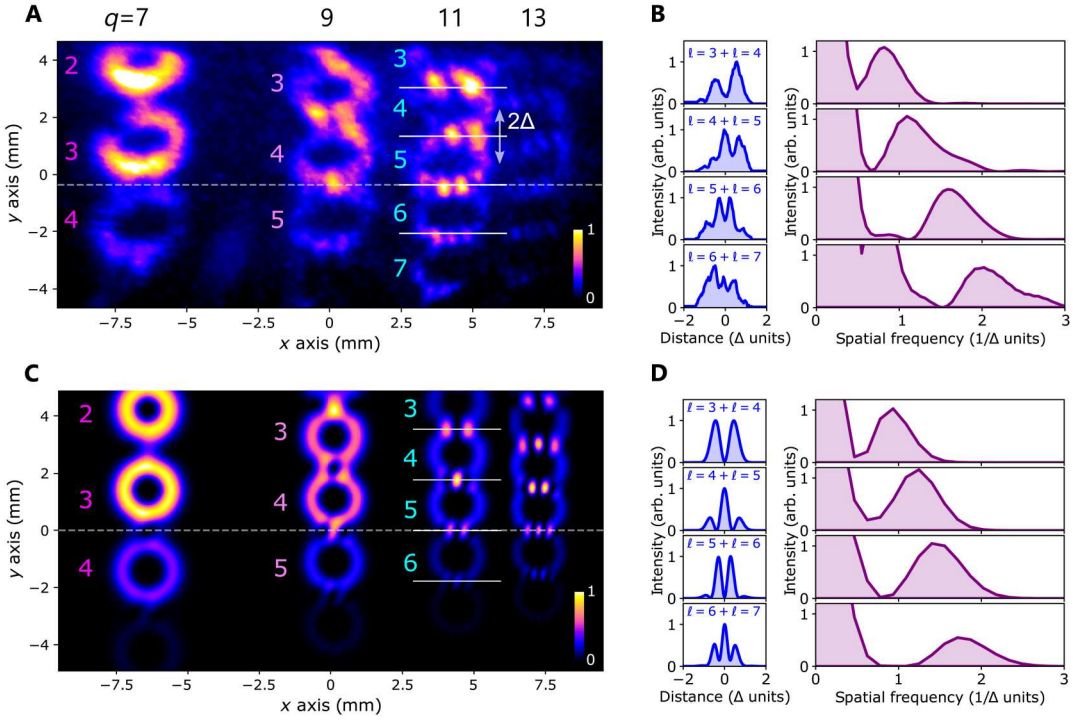

Fig. 2. High harmonic spectrum generated by a combination of ℓ_1=0 and ℓ_2=1 linearly polarized noncollinear driving beams. (**A**) Experimental intensity profiles of harmonics 7, 9, 11, and 13. The colored digits indicate the OAM charge of the nearest XUV vortex. The bisector of the driving beams is indicated with a horizontal dashed line. Δ is half the distance between the centers of two neighboring vortices, which only depends on the harmonic order and the relative angle θ of the driving beams. (**B**) Line outs of harmonic 11 along the white horizontal lines in (A) (left) and corresponding spatial Fourier transform (right), with spatial frequencies in units of 1/Δ. (**C**) Simulated intensity profiles of harmonics 7, 9, 11, and 13. (**D**) Line outs of harmonic 11 along the white horizontal lines in (C) (left) and corresponding spatial Fourier transform (right).

yielding $j_\gamma^{(7)} = 7/2, j_\gamma^{(9)} = 9/2, j_\gamma^{(11)} = 11/2$, and so on. This trend is shown in Fig. 4. In collinear driving geometry, where the $\sigma_\pm^{(q)} = \pm 1$ beamlets are both emitted on axis, the GAM charge is well defined and varies linearly with the harmonic order, while the OAM and SAM each have two contributions for each harmonic.

In the absence of a spectrometer in the setup, the XUV emission depicted in Fig. 3 would simply consist of two broadband XUV rings separated angularly, with opposite helicity, each ring being a comb of harmonics with increasing OAM values. Thus, in the temporal domain, this noncollinear scheme allows the simultaneous generation of right and left circularly polarized attosecond light springs (*8*, *17*, *29*). Here, we use simulations based on the strong-field approximation (SFA) to visualize the spatiotemporal structure of the XUV light (see the "Spatio-temporal profile of the HHG emission in the noncollinear scheme" section in Supplementary Text) and find that each of the two light springs exhibits a single helix. This is reminiscent of the fact that the transverse profile of a beam with $j_\gamma = \frac{1}{2}$ only contains one single amplitude extremum at any given time (Fig. 1A). On the contrary, regular LG beams exhibit an even number of extrema in their profile and yield attosecond light springs with an even number of helices (*17*, *29*).

DISCUSSION

We experimentally demonstrated that the GAM charge j_γ is conserved in nonlinear optics and that the topology of the fundamental field is transferred to the generated light. Using the eigenstates of the GAM operator as the basis of the laser modes, we turned the combined OAM/SAM parametric conservation laws, which yield harmonics with ill-defined angular momenta, into a linear scaling of the GAM charge. j_γ is thus the appropriate quantum number to describe nonlinear phenomena involving light fields invariant under coordinated rotations. We also note that because the eigenstates of the GAM (i.e., polarization Möbius strips and twisted ribbons) coincide with nonseparable spin-orbit states (*24*), our work shows that HHG preserves the nonseparability of the SAM and OAM degrees of freedom of the photons by transferring the polarization Möbius strip structure to the high harmonics.

Incidentally, we directly observed the interference between two photon channels contributing to the same harmonic order. Our scheme could thus contribute to the validation of photon-based theories of HHG (*40*). By exploiting transverse mode conversion by astigmatic focusing, we also introduced an OAM measurement method in the XUV that is of general usefulness. It may serve the ever growing interest in applications of focused harmonic beams carrying OAM, SAM, or both, for instance, in angular momentum–induced dichroisms (*41*–*43*). The production of XUV light beams with fractional-order polarization singularities also opens more perspectives in ultrafast light-matter interaction. In particular, the control of light's topology at ultrafast time scales could lead to light beams with time-varying nontrivial GAM ($\gamma \neq 0$), along the lines of (*44*), or beams with a dynamical symmetry (*45*, *46*) and be extended to bichromatic fields (*20*, *47*, *48*), HHG driven by

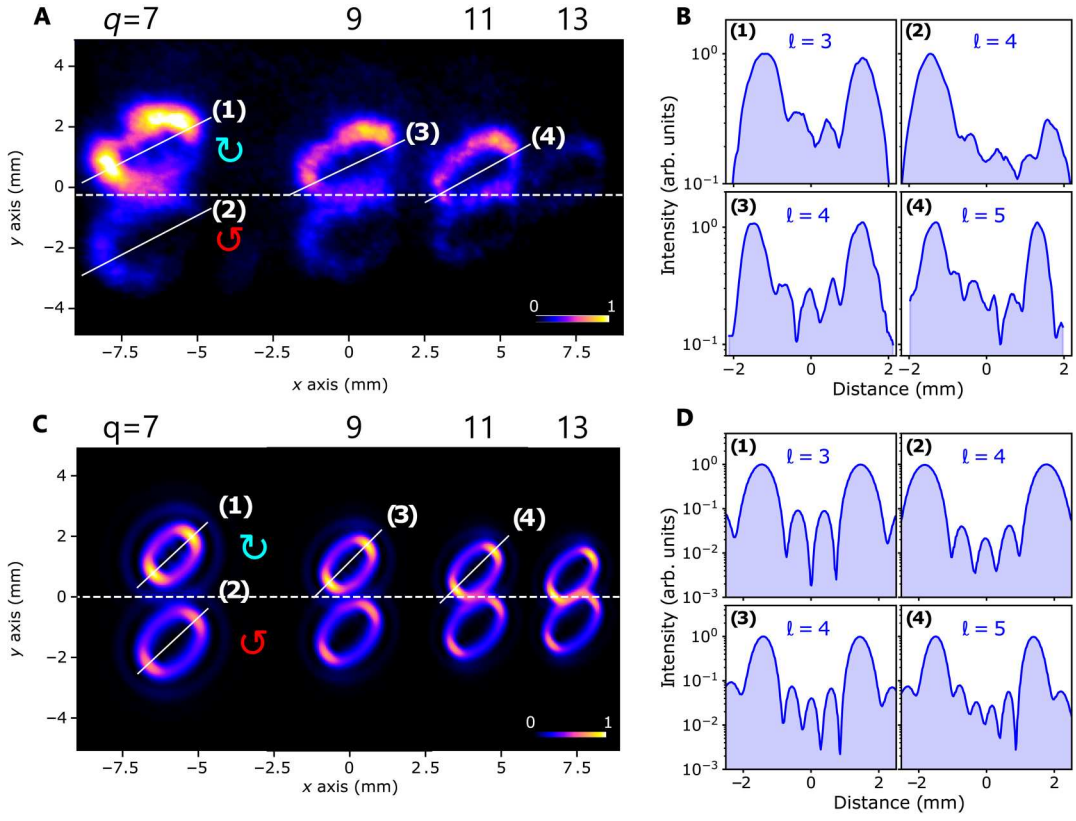

Fig. 3. High harmonic spectrum obtained with a polarization Möbius strip as the driving field. (**A**) Experimental intensity profiles of harmonics 7, 9, 11, and 13. The bisector of the driving beams is indicated with a horizontal dashed line. Circular arrows indicate the SAM of the light above and below the bisector (blue, $\sigma = +1$ emission channel; red, $\sigma = -1$ emission channel). The two beamlets of each harmonic order have unequal intensity because the two driving beams have unequal pulse energy. (**B**) Line outs of the XUV intensity along the corresponding lines in (A) in log scale. The number of intensity minima corresponds to the OAM charge of the vortex considered. (**C**) Simulated intensity profiles of harmonics 7, 9, 11, and 13. To simulate the astigmatism of the optical setup, we impose a spatial phase varying quadratically with the *y* coordinate to the XUV field before propagation. (**D**) Line outs of the XUV intensity along the corresponding lines in (C) in log scale.

single-cycle pulses (*49*), tightly focused fields (*50*), and HHG in nonlinear media with broken rotational symmetry (*51*), further expanding the capabilities of ultrafast angular momentum-based spectroscopy. Last, our results, combined with the recent progress of the quantum optical description of HHG (*52*), could enlighten the discussion triggered by Ballantine *et al.* (*2*) about the photon statistics of light beams with noninteger angular momentum.

MATERIALS AND METHODS

Experimental setup

The fundamental laser is a Ti:sapphire regenerative amplifier, delivering 25-fs pulses centered at an 800-nm wavelength, with a 1-kHz repetition rate and a 2-mJ pulse energy. The laser is split in two beams (beams 1 and 2) by an intensity beam splitter and propagates in a Mach-Zender interferometer (see the "Experimental setup" section in Supplementary Text). A spiral phase plate (SPP), made of 16 azimuthal steps and manufactured by SILIOS Technologies, gives an OAM charge $\ell_2 = 1$ to beam 2 (see the "Measurement of the topological charge carried by beam 2" section in Supplementary Text). The SPP is designed to imprint an optical path varying from 0 to $\lambda_{IR} = 800$ nm over a 2π azimuthal range. At the output of the interferometer, the two beams are recombined noncollinearly. Their relative angle θ is kept sufficently small (50 mrad) to remain in the paraxial regime and avoid any spin-orbit coupling of light (*11*). A zero-order half waveplate (HWP) is placed in beam 2, and a zero-order quarter waveplate (QWP) is common to both beams after the interferometer. To obtain counter-rotating circular IR beams, the slow axis of the HWP is precisely aligned at 45° so that the field of beam 2 becomes horizontally polarized, and the axis of the QWP common to both beams is precisely set at 45° (see the "Gaussian counter-rotating circularly polarized drivers" section in Supplementary Text). Each beam (collimated and apertured with an iris of 14 mm in diameter) is focused using a plano-convex lens with 75-cm focal length. The diameter of the focal spot size is about 50 μm. After passing through all the optical elements, a pulse of beam 1 (respectively, beam 2) has an energy of 0.61 mJ (respectively, 0.52 mJ). The optical path difference between the interferometer's arms is set to zero by means of a delay stage placed in beam 1. HHG occurs in an effusive jet of argon atoms issued from a 500-μm nozzle located in the focal plane of both beams. To observe the intervortex interference or to achieve controllable LG-to-HG mode conversion, astigmatism must be limited, which prevents the use of cylindrical mirrors and gratings with variable steps that are commonly used in HHG experiments. We use instead a gold grating with uniform periodicity (600 grooves/mm). The XUV spot size on the grating must be minimized to limit dispersion. The harmonics are thus focused by a near normal incidence spherical mirror with boron carbide

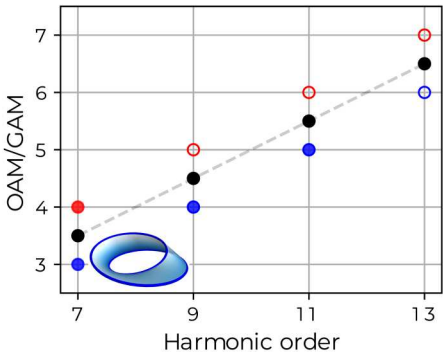

Fig. 4. Linear scaling of the GAM. Each harmonic order q is in a superposition of two modes of OAM $(q-1)/2$ and $(q+1)/2$, with SAM +1 (blue circles) and −1 (red circles), respectively. The GAM charge, defined as $j_{1/2} = \ell + \frac{1}{2}\sigma$, is shown with black dots. The red and blue dots that are filled correspond with the OAM measured by LG-to-HG mode conversion, while the empty ones show the measurement based on XUV vortices interference (performed in linearly polarized light). The inset 3D surface illustrates the Möbius strip topology of the harmonics generated in collinear geometry.

(B_4C) coating and 600-mm curvature radius. The angle of incidence on the mirror allows us to control the astigmatism as per requirement. The near-normal incidence reflections on the spherical mirror and the grating prevent efficient detection of wavelength shorter than 50 nm, which approximately corresponds to harmonic order 15 (see the "Experimental setup" section in Supplementary Text). The harmonics propagate to the far field where a set of microchannel plates and a phosphor screen is located. Last, the XUV spectrum at the back of the phosphor screen is recorded with a complementary metal-oxide semiconductor camera (Hamamatsu Photonics, model ORCA Spark C11440-36 U). The experimental images shown in this work were acquired by averaging 30 frames, with 0.6-s exposure time for each frame.

HHG simulations

The numerical model [the so-called "thin-slab model" (*53*)] assumes that the gas jet is infinitely thin in the longitudinal direction so that HHG occurs in a 2D transverse plane. Thus, we discard any longitudinal phase-matching effect. This gas sheet is placed at the crossing point of the two driving beams, where their respective foci are located. The intensity of the HHG emission in the focal plane is computed as $I_{\mathrm{IR}}^{q_{\mathrm{eff}}} e^{-\left(\frac{\epsilon_{\mathrm{IR}}}{\epsilon_0}\right)^2}$, where I_{IR} is the local intensity of the IR field (with a peak intensity of 10^{14} W cm^{-2}), $q_{\mathrm{eff}} = 3.5$ is a typical effective order of nonlinearity (*53*), and ϵ_{IR} and $\epsilon_0 = 0.2$ are the local ellipticity of the IR and a threshold ellipticity, respectively (*27*). The phase of the harmonic order q at the focus is given by $q\phi_{\mathrm{IR}} + \alpha_{\mathrm{at}} I_{\mathrm{IR}}$, with ϕ_{IR} as the local phase of the IR field and $\alpha_{\mathrm{at}} I_{\mathrm{IR}}$ as the atomic phase, proportional to the IR intensity. The strong-field parameter $\alpha_{\mathrm{at}} = 2 \times 10^{-14}$ cm^2 W^{-1} corresponds to short electronic trajectories. The polarization state of the generated harmonics at focus is assumed to exactly match that of the IR. The resulting XUV field is then propagated to the far field using the Fraunhofer propagation operator (*53*). In the simulation, the first beam is an ideal right circularly polarized Gaussian beam, and the second beam is an ideal left circularly polarized LG mode of indices ($\ell = 1$, $\rho = 0$), both having the same waist radius $w_0 = 50$ μm. The peak intensity of the LG beam is 0.85 times that of the Gaussian beam. The noncollinear angle θ is adjusted so that, in the far field, the distance Δ between two XUV vortices matches with the experiment (we did not simulate the effect of the refocusing optics on the relative angle of the beamlets). This configuration is achieved for θ = 40 mrad in the simulation. Quantum simulations based on the SFA were also performed to corroborate the temporal emission of the Möbius strip driven harmonics in the form of circularly polarized attosecond light springs (see the "Spatio-temporal profile of the HHG emission in the non-collinear scheme" in Supplementary Text).

Supplementary Materials

This PDF file includes:
Supplementary Text
Figs. S1 to S13
Legend for movie S1
References

Other Supplementary Material for this manuscript includes the following:
Movie S1

REFERENCES AND NOTES

1. D. Arovas, J. R. Schrieffer, F. Wilczek, Fractional statistics and the quantum hall effect. *Phys. Rev. Lett.* **53**, 722 (1984).
2. K. E. Ballantine, J. F. Donegan, P. R. Eastham, There are many ways to spin a photon: Half-quantization of a total optical angular momentum. *Sci. Adv.* **2**, e1501748 (2016).
3. E. Pisanty, G. J. Machado, V. Vicuña-Hernández, A. Picón, A. Celi, J. P. Torres, M. Lewenstein, Knotting fractional order knots with the polarization state of light. *Nat. Photonics* **13**, 569–574 (2019).
4. I. Freund, Cones, spirals, and Möbius strips, in elliptically polarized light. *Opt. Commun.* **249**, 7–22 (2005).
5. I. Freund, Multitwist optical Möbius strips. *Opt. Lett.* **35**, 148–150 (2010).
6. E. J. Galvez, I. Dutta, K. Beach, J. J. Zeosky, J. A. Jones, B. Khajavi, Multitwist Möbius strips and twisted ribbons in the polarization of paraxial light beams. *Sci. Rep.* **7**, 13653 (2017).
7. J. B. Götte, K. O'Holleran, D. Preece, F. Flossmann, S. Franke-Arnold, S. M. Barnett, M. J. Padgett, Light beams with fractional orbital angular momentum and their vortex structure. *Opt. Express* **16**, 993–1006 (2008).
8. A. Turpin, L. Rego, A. Picón, J. San Román, C. Hernández-García, Extreme ultraviolet fractional orbital angular momentum beams from high harmonic generation. *Sci. Rep.* **7**, 43888 (2017).
9. E. Pisanty, L. Rego, J. San Román, A. Picón, K. M. Dorney, H. C. Kapteyn, M. M. Murnane, L. Plaja, M. Lewenstein, C. Hernández-García, Conservation of torus-knot angular momentum in high-order harmonic generation. *Phys. Rev. Lett.* **122**, 203201 (2019).
10. A. de las Heras, A. K. Pandey, J. S. Román, J. Serrano, E. Baynard, G. Dovillaire, M. Pittman, C. G. Durfee, L. Plaja, S. Kazamias, O. Guilbaud, C. Hernández-García, Extreme-ultraviolet vector-vortex beams from high harmonic generation. *Optica* **9**, 71–79 (2022).
11. K. Y. Bliokh, F. J. Rodríguez-Fortuño, F. Nori, A. V. Zayats, Spin-orbit interactions of light. *Nat. Photonics* **9**, 796–808 (2015).
12. B. P. da Silva, W. T. Buono, L. J. Pereira, D. S. Tasca, K. Dechoum, A. Z. Khoury, Spin to orbital angular momentum transfer in frequency up-conversion. *Nanophotonics* **11**, 8 (2021).
13. D. M. Villeneuve, Attosecond science. *Contemp. Phys.* **59**, 47–61 (2018).
14. A. McPherson, G. Gibson, H. Jara, U. Johann, T. S. Luk, I. A. McIntyre, K. Boyer, C. K. Rhodes, Studies of multiphoton production of vacuum-ultraviolet radiation in the rare gases. *J. Opt. Soc. Am. B* **4**, 595–601 (1987).
15. M. Ferray, A. L'Huillier, X. F. Li, L. A. Lompre, G. Mainfray, C. Manus, Multiple-harmonic conversion of 1064 nm radiation in rare gases. *Mol. Opt. Phys.* **21**, L31–L35 (1988).
16. G. Gariepy, J. Leach, K. T. Kim, T. J. Hammond, E. Frumker, R. W. Boyd, P. B. Corkum, Creating high-harmonic beams with controlled orbital angular momentum. *Phys. Rev. Lett.* **113**, 153901 (2014).
17. R. Géneaux, A. Camper, T. Auguste, O. Gobert, J. Caillat, R. Taïeb, T. Ruchon, Synthesis and characterization of attosecond light vortices in the extreme ultraviolet. *Nat. Commun.* **7**, 12583 (2016).
18. F. Kong, C. Zhang, F. Bouchard, Z. Li, G. G. Brown, D. H. Ko, T. J. Hammond, L. Arissian, R. W. Boyd, E. Karimi, P. B. Corkum, Controlling the orbital angular momentum of high harmonic vortices. *Nat. Commun.* **8**, 14970 (2017).

19. D. Gauthier, P. R. Ribič, G. Adhikary, A. Camper, C. Chappuis, R. Cucini, L. F. Dimauro, G. Dovillaire, F. Frassetto, R. Géneaux, P. Miotti, L. Poletto, B. Ressel, C. Spezzani, M. Stupar, T. Ruchon, G. de Ninno, Tunable orbital angular momentum in high-harmonic generation. *Nat. Commun.* **8**, 14971 (2017).
20. K. M. Dorney, L. Rego, N. J. Brooks, J. San Román, C.-T. Liao, J. L. Ellis, D. Zusin, C. Gentry, Q. L. Nguyen, J. M. Shaw, A. Picón, L. Plaja, H. C. Kapteyn, M. M. Murnane, C. Hernández-García, Controlling the polarization and vortex charge of attosecond high-harmonic beams via simultaneous spin-orbit momentum conservation. *Nat. Photon.* **13**, 123–130 (2019).
21. L. Allen, M. W. Beijersbergen, R. J. C. Spreeuw, J. P. Woerdman, Orbital angular momentum of light and the transformation of laguerre-gaussian laser modes. *Phys. Rev. A* **45**, 8185–8189 (1992).
22. A. T. O'Neil, J. Courtial, Mode transformations in terms of the constituent Hermite–Gaussian or Laguerre–Gaussian modes and the variable-phase mode converter. *Optics Commun.* **181**, 35–45 (2000).
23. M. J. Padgett, L. Allen, The angular momentum of light: Optical spanners and the rotational frequency shift. *Opt. Quantum Electron.* **31**, 1–12 (1999).
24. C. V. S. Borges, M. Hor-Meyll, J. A. O. Huguenin, A. Z. Khoury, Bell-like inequality for the spin-orbit separability of a laser beam. *Phys. Rev. A* **82**, 033833 (2010).
25. J. F. Nye, Lines of circular polarization in electromagnetic wave fields. *Proc. R. Soc. Lond. A Math. Phys. Sci.* **389**, 279–290 (1983).
26. M. V. Berry, Index formulae for singular lines of polarization. *J. Opt. A Pure Appl. Opt.* **6**, 675–678 (2004).
27. K. S. Budil, P. Salières, A. L'Huillier, T. Ditmire, M. D. Perry, Influence of ellipticity on harmonic generation. *Phys. Rev. A* **48**, R3437–R3440 (1993).
28. N. Bloembergen, Conservation laws in nonlinear optics∗. *J. Opt. Soc. Am.* **70**, 1429 (1980).
29. C. Hernández-García, A. Picón, J. San Román, L. Plaja, Attosecond extreme ultraviolet vortices from high-order harmonic generation. *Phys. Rev. Lett.* **111**, 083602 (2013).
30. A. Fleischer, O. Kfir, T. Diskin, P. Sidorenko, O. Cohen, Spin angular momentum and tunable polarization in high-harmonic generation. *Nat. Photon.* **8**, 543–549 (2014).
31. E. Pisanty, S. Sukiasyan, M. Ivanov, Spin conservation in high-order-harmonic generation using bicircular fields. *Phys. Rev. A* **90**, 043829 (2014).
32. O. E. Alon, V. Averbukh, N. Moiseyev, Selection rules for the high harmonic generation spectra. *Phys. Rev. Lett.* **80**, 3743–3746 (1998).
33. M. Dennis, Polarization singularities in paraxial vector fields: Morphology and statistics. *Opt. Commun.* **213**, 201–221 (2002).
34. B. Vodungbo, A. B. Sardinha, J. Gautier, G. Lambert, C. Valentin, M. Lozano, G. Iaquaniello, F. Delmotte, S. Sebban, J. Lüning, P. Zeitoun, Polarization control of high order harmonics in the EUV photon energy range. *Opt. Express* **19**, 4346–4356 (2011).
35. F. Siegrist, J. A. Gessner, M. Ossiander, C. Denker, Y.-P. Chang, M. C. Schröder, A. Guggenmos, Y. Cui, J. Walowski, U. Martens, J. K. Dewhurst, U. Kleineberg, M. Münzenberg, S. Sharma, M. Schultze, Light-wave dynamic control of magnetism. *Nature* **571**, 240–244 (2019).
36. F. Sanson, A. K. Pandey, F. Harms, G. Dovillaire, E. Baynard, J. Demailly, O. Guilbaud, B. Lucas, O. Neveu, M. Pittman, D. Ros, M. Richardson, E. Johnson, W. Li, P. Balcou, S. Kazamias, Hartmann wavefront sensor characterization of a high charge vortex beam in the extreme ultraviolet spectral range. *Opt. Lett.* **43**, 2780–2783 (2018).
37. J. B. Bertrand, H. J. Wörner, H.-C. Bandulet, E. Bisson, M. Spanner, J.-C. Kieffer, D. M. Villeneuve, P. B. Corkum, Ultrahigh-order wave mixing in noncollinear high harmonic generation. *Phys. Rev. Lett.* **106**, 023001 (2011).
38. D. D. Hickstein, F. J. Dollar, P. Grychtol, J. L. Ellis, R. Knut, C. Hernández-García, D. Zusin, C. Gentry, J. M. Shaw, T. Fan, K. M. Dorney, A. Becker, A. Jaron-Becker, H. C. Kapteyn, M. M. Murnane, C. G. Durfee, Non-collinear generation of angularly isolated circularly polarized high harmonics. *Nat. Photon.* **9**, 743–750 (2015).
39. P. Vaity, J. Banerji, R. Singh, Measuring the topological charge of an optical vortex by using a tilted convex lens. *Phys. Lett. A* **377**, 1154–1156 (2013).
40. L. Li, P. Lan, L. He, X. Zhu, J. Chen, P. Lu, Scaling law of high harmonic generation in the framework of photon channels. *Phys. Rev. Lett.* **120**, 223203 (2018).
41. X. Zambrana-Puyalto, X. Vidal, G. Molina-Terriza, Angular momentum-induced circular dichroism in non-chiral nanostructures. *Nat. Commun.* **5**, 4922 (2014).
42. K. A. Forbes, D. L. Andrews, Orbital angular momentum of twisted light: Chirality and optical activity. *J. Phys. Photon.* **3**, 022007 (2021).
43. M. Fanciulli, M. Pancaldi, E. Pedersoli, M. Vimal, D. Bresteau, M. Luttmann, D. De Angelis, P. R. Ribič, B. Rösner, C. David, C. Spezzani, M. Manfredda, R. Sousa, I.-L. Prejbeanu, L. Vila, B. Dieny, G. De Ninno, F. Capotondi, M. Sacchi, T. Ruchon, Observation of magnetic helicoidal dichroism with extreme ultraviolet light vortices. *Phys. Rev. Lett.* **128**, 077401 (2022).
44. L. Rego, K. M. Dorney, N. J. Brooks, Q. L. Nguyen, C.-T. Liao, J. San Román, D. E. Couch, A. Liu, E. Pisanty, M. Lewenstein, L. Plaja, H. C. Kapteyn, M. M. Murnane, C. Hernández-García, Generation of extreme-ultraviolet beams with time-varying orbital angular momentum. *Science* **364**, eaaw9486 (2019).
45. O. Neufeld, D. Ayuso, P. Decleva, M. Y. Ivanov, O. Smirnova, O. Cohen, Ultrasensitive chiral spectroscopy by dynamical symmetry breaking in high harmonic generation. *Phys. Rev. X* **9**, 031002 (2019).
46. G. Lerner, O. Neufeld, L. Hareli, G. Shoulga, E. Bordo, A. Fleischer, D. Podolsky, A. Bahabad, O. Cohen, Multi-scale dynamical symmetries and selection rules in nonlinear optics. arXiv:2109.01941 [physics.optics] (21 September 2021).
47. F. Kong, C. Zhang, H. Larocque, F. Bouchard, Z. Li, M. Taucer, G. Brown, S. Severino, T. J. Hammond, E. Karimi, P. B. Corkum, Spin-constrained orbital-angular-momentum control in high-harmonic generation. *Phys. Rev. Res.* **1**, 032008 (2019).
48. W. Paufler, B. Böning, S. Fritzsche, Tailored orbital angular momentum in high-order harmonic generation with bicircular laguerre-gaussian beams. *Phys. Rev. A* **98**, 011401 (2018).
49. P.-C. Huang, C. Hernández-García, J.-T. Huang, P.-Y. Huang, C.-H. Lu, L. Rego, D. D. Hickstein, J. L. Ellis, A. Jaron-Becker, A. Becker, S.-D. Yang, C. G. Durfee, L. Plaja, H. C. Kapteyn, M. M. Murnane, A. H. Kung, M.-C. Chen, Polarization control of isolated high-harmonic pulses. *Nat. Photon.* **12**, 349–354 (2018).
50. Y. Fang, M. Han, P. Ge, Z. Guo, X. Yu, Y. Deng, C. Wu, Q. Gong, Y. Liu, Photoelectronic mapping of the spin-orbit interaction of intense light fields. *Nat. Photon.* **15**, 115–120 (2021).
51. Y. S. You, D. A. Reis, S. Ghimire, Anisotropic high-harmonic generation in bulk crystals. *Nat. Phys.* **13**, 345–349 (2017).
52. M. Lewenstein, M. F. Ciappina, E. Pisanty, J. Rivera-Dean, P. Stammer, T. Lamprou, P. Tzallas, Generation of optical Schrödinger cat states in intense laser-matter interactions. *Nat. Phys.* **17**, 1104–1108 (2021).
53. L. Rego, J. S. Román, L. Plaja, A. Picón, C. Hernández-García, Ultrashort extreme ultraviolet vortices, in *Vortex Dynamics and Optical Vortices*, H. P. de Tejada, Ed. (IntechOpen, 2017), chap. 9.
54. J. Ma, P. Li, Z. Zhou, Y. Gu, Characteristics of fork-shaped fringes formed by off-axis interference of two vortex beams. *J. Opt. Soc. Am. A* **38**, 115–123 (2021).
55. R. Géneaux, C. Chappuis, T. Auguste, S. Beaulieu, T. T. Gorman, F. Lepetit, L. F. DiMauro, T. Ruchon, Radial index of Laguerre-Gaussian modes in high-order-harmonic generation. *Phys. Rev. A* **95**, 051801 (2017).
56. I. Kimel, L. R. Elias, Relations between hermite and laguerre gaussian modes. *IEEE J. Quantum Electron.* **29**, 2562–2567 (1993).
57. M. A. Bandres, J. C. Gutiérrez-Vega, Ince–Gaussian beams. *Opt. Lett.* **29**, 144 (2004).
58. C. Hernández-García, J. A. Pérez-Hernández, J. Ramos, E. C. Jarque, L. Roso, L. Plaja, High-order harmonic propagation in gases within the discrete dipole approximation. *Phys. Rev. A* **82**, 033432 (2010).
59. H. Ruf, "Dynamique moléculaire par imagerie attoseconde," thesis, Université Bordeaux 1 (2012).

Acknowledgments

Funding: This work was supported by the French "Investments for the Future" of the Agence Nationale pour la Recherche (contract nos. 11-EQPX0005-ATTOLAB, ANR-14-CE32-0010 - Xstase, ANR-10-LABX-0039-PALM ATTO-Foam, and ANR HELIMAG ANR-21-CE30-0037), the Scientific Cooperation Foundation of Paris-Saclay University through the funding of the OPT2X research project (Lidex 2014), the Île-de-France region through the Pulse-X project, and the European Union's Horizon 2020 Research and Innovation Program no. EU-H2020-LASERLAB-EUROPE654148. E.P. acknowledges support by the Royal Society through the University Research Fellowship URF\R1\211390. C.H.-G. acknowledges support from the European Research Council (ERC) under the European Union's Horizon 2020 Research and Innovation Program (grant agreement no. 851201), Ministerio de Ciencia e Innovación (RYC-2017-22745, PID2019-106910GB-I00), and Junta de Castilla y León (SA287P18). A.Z.K. acknowledges funding from Fundação Carlos Chagas Filho de Amparo à Pesquisa do Estado do Rio de Janeiro (FAPERJ), Instituto Nacional de Ciência e Tecnologia de Informação Quântica (INCT-IQ 465469/2014-0), Fundação de Amparo à Pesquisa do Estado de São Paulo (FAPESP, grant 2021/06823-5). **Author contributions:** M.L., M.V., and T.R. conceived the experiment. M.L., M.V., and J.-F.H. performed the experiment and collected the data. M.L. analyzed the data. M.G. and C.H.-G. performed the simulations. M.L., T.R., E.P., C.H.-G., A.Z.K., and M.G. interpreted the results. M.L. and T.R. wrote the manuscript with contributions from all authors. **Competing interests:** The authors declare that they have no competing interests. **Data and materials availability:** All data needed to evaluate the conclusions in the paper are present in the paper and/or the Supplementary Materials.

Submitted 20 October 2022
Accepted 23 February 2023
Published 24 March 2023
10.1126/sciadv.adf3486